A machine learning driven 3D+1D model for efficient characterization of proton exchange membrane fuel cells

Pan, Y., Ruan, H., Wu, B., Regmi, Y. N., Wang, H. & Brandon, N. P

DOI 10.1016/j.egyai.2024.100397
ESSN 2666-5468

Publisher: Elsevier

Energy and AI 17 (2024) 100397

Contents lists available at ScienceDirect

Energy and AI

journal homepage: www.sciencedirect.com/journal/energy-and-ai

A machine learning driven 3D+1D model for efficient characterization of proton exchange membrane fuel cells

Yuwei Pan [a,1], Haijun Ruan [b,c,1], Billy Wu [b], Yagya N. Regmi [d,*], Huizhi Wang [e,*], Nigel P. Brandon [a,*]

[a] Department of Earth Science and Engineering, Imperial College London, London SW7 2AZ, UK
[b] Dyson School of Design Engineering, Imperial College London, London SW7 2AZ, UK
[c] Centre for E-Mobility and Clean Growth, Coventry University, Coventry CV1 5FB, UK
[d] Manchester Fuel Cell Innovation Centre, Department of Natural Sciences, Manchester Metropolitan University, Manchester M1 5GD, UK
[e] Department of Mechanical Engineering, Imperial College London, London SW7 2AZ, UK

HIGHLIGHTS

- A neural network driven model is presented for proton exchange membrane fuel cells.
- The experimental results are replicated with high accuracy.
- Computational speed matches existing hierarchical models with preserved nonlinearity.
- High gas flow rate can be detrimental to fuel cell performance under low humidity.
- 80% of anode catalyst layer is found to generate little current, especially near the inlet.

GRAPHICAL ABSTRACT

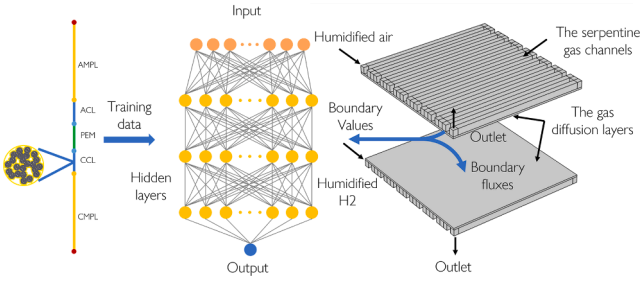

ARTICLE INFO

Keywords:
Proton exchange membrane fuel cell
Hierarchical model
Neural network
Hybrid model

ABSTRACT

The computational demands of 3D continuum models for proton exchange membrane fuel cells remain substantial. One prevalent approach is the hierarchical model combining a 2D/3D flow field with a 1D sub-model for the catalyst layers and membrane. However, existing studies often simplify the 1D domain to a linearized 0D lumped model, potentially resulting in significant errors at high loads. In this study, we present a computationally efficient neural network driven 3D+1D model for proton exchange membrane fuel cells. The 3D sub-model captures transport in the gas channels and gas diffusion layers and is coupled with a 1D electrochemical sub-model for microporous layers, membrane, and catalyst layers. To reduce computational intensity of the full 1D description, a neural network surrogates the 1D electrochemical sub-model for coupling with the 3D domain. Trained by model-generated large synthetic datasets, the neural network achieves root mean square errors of less than 0.2%. The model is validated against experimental results under various relative humidities. It is then employed to investigate the nonlinear distribution of internal states under different operating conditions. With the neural network operating at 0.5% of the computing cost of the 1D sub-model, the hybrid model preserves a detailed and nonlinear representation of the internal fuel cell states while maintaining computational costs comparable to conventional 3D+0D models. The presented hybrid data-driven and physical modeling

* Corresponding authors.
E-mail addresses: y.regmi@mmu.ac.uk (Y.N. Regmi), huizhi.wang@imperial.ac.uk (H. Wang), n.brandon@imperial.ac.uk (N.P. Brandon).
[1] These authors contributed to the work equally.

https://doi.org/10.1016/j.egyai.2024.100397

Available online 14 July 2024

framework offers high accuracy and computing speed across a broad spectrum of operating conditions, potentially aiding the rapid optimization of both the membrane electrode assembly and the gas channel geometry.

Nomenclature

Symbols

a	Specific surface area, $m^2\ m^{-3}$
c	Concentration, mol m^{-3}
C_p	Heat capacity, J $kg^{-1}\ K^{-1}$
d	Diameter, m
D	Diffusion coefficients, $m^2\ s^{-1}$
Er	Agglomerate effective factor
f	Ionomer water volume fraction
F	Faraday constant, C mol^{-1}
h	Henry's constant, Pa $m^3\ mol^{-1}$
H	Enthalpy, kJ mol^{-1}
i	Local volumetric current density or exchange current density, A m^{-3} or A cm^{-2}
I	Output current density, A m^{-2}
j	Flux, A m^{-2}, mol $m^{-2}\ s^{-1}$, W m^{-2}
k	Thermal conductivity, W $m^{-1}\ K^{-1}$
K	Permeability, m^2
M	Molar mass, kg mol^{-1}
P	Pressure, Pa
q	Cathode half-cell reaction coefficient, s^{-1}
R	Gas constant, J $mol^{-1}\ K^{-1}$
RH	Relative humidity
s	Liquid water saturation
S	Source term
ΔS	Entropy change, J $mol^{-1}\ K^{-1}$
t	Time, s
T	Temperature, K
u	Fluid velocity, m s^{-1}
U	Potential, V
v	Volume flow rate, $m^3\ s^{-1}$
V	Molar volume or, $m^3\ mol^{-1}$
X	Molar fraction
Y	Mass fraction

Greeks

β	Thiele modulus
γ	Evaporation/condensation coefficient, s^{-1}
δ	Film thickness, m
ε	Volume fraction
η	Overpotential, V
θ	Coverage ratio
κ	Liquid water permeability, m^2
λ	Ionomer water content
μ	Viscosity, mPa s
ξ	Electro-osmotic drag coefficient
ρ	Density, kg m^{-3}
σ	Electron/proton conductivity, S m^{-1}
τ	Tortuosity
ϕ	Potential, V

Subscripts

0	Reference
a	Anode
ad	Adsorption/desorption
agg	Agglomerate
c	Cathode
cc	Current collector
cell	Fuel cell
CH	Channel
e^-	Electron
ec	Evaporation/condensation
eff	Effective
film	Ionomer film
g	Gas
H_2	Hydrogen
H_2O	Water
HOR	Hydrogen oxidation reaction
i	Species
l	Liquid water
m	Mass
NN	Neural network
o	Outlet
O_2	Oxygen
p	Pore
P	Proton
PtO	Platinum oxide
ref	Reference
sat	Saturated
T	Temperature
w	Liquid water
λ	Ionomer water content

Abbreviations

BP	Bipolar plate
CL	Catalyst layer
ECSA	Electrochemical surface area
GDL	Gas diffusion layer
HOR	Hydrogen oxidation reaction
LSTM	Long short-term memory network
MEA	Membrane electrode assembly
MSE	Mean square error
NN	Neural network
ODE	Ordinary differential equation
ORR	Oxygen reduction reaction
PDE	Partial differential equation
PSO	Particle swarm optimization
PEMFC	Proton exchange membrane fuel cell
RH	Relative humidity
RMSE	Root mean square error
RSA	Response surface approximation

1. Introduction

Proton exchange membrane fuel cells (PEMFCs) use hydrogen as a fuel to generate electricity with zero local carbon emissions and are considered a promising energy conversion device for the clean energy economy [1]. However, the widespread commercialization of PEMFCs still faces several challenges, which include achieving higher performance, reducing costs, and enhancing durability [2]. Over the last few decades, numerous efforts have been made to improve PEMFCs, with numerical models extensively used for understanding physicochemical processes inside cells and optimizing their designs [3].

Existing PEMFC models can be classified into three categories [4]:

empirical, physical, and data-driven models. A typical empirical model describes the polarization losses, including the ohmic, activation, and concentration losses [5]. Empirical models can be fitted to the polarization curves measured by experiments and have very low computational cost, but their accuracy is limited to narrow ranges of operating conditions [6]. However, despite the lack of generalizability, the low computational demand has resulted in the use of empirical models in many aspects of fuel cells, such as lifetime prediction [7] and system control [8].

On the other hand, physics-based continuum models solve partial differential equations (PDEs) or ordinary differential equations (ODEs) for the physicochemical processes inside a fuel cell, and they usually have high accuracy under wider ranges of operating conditions. The continuum models can be categorized based on their dimensionality [6], which can be 1D [9], 2D [10], or 3D [11]. Using a 1D model [12], Vetter and Schumacher [13] conducted a parametric study on the sensitivity of the material properties. Five membrane properties, including: membrane hydration–water activity relationship, electro-osmotic drag coefficient, membrane thickness, membrane water diffusion coefficient, and proton transport resistance, were found to be the most influential parameters [14]. However, their model potentially underestimates the influence of oxygen transport properties due to the ignored gradient in the gas channels and the ionomer. Based on the conventional 1D PEMFC models, Wang et al. [9] developed a 1D model with catalyst layer (CL) agglomerates and ionomer film. The model was used to analyze the effects of oxygen and proton transport under different conditions, but the electro-osmotic drag was ignored. Zhang et al. [15] compared the simulation results of 1D and 3D models, finding that despite using consistent physical parameters, the 1D model tends to predict significantly higher voltage, even when considering a single channel. Compared to empirical models, the 1D models included the heterogeneity in the thickness direction at the cost of a several magnitudes longer computing time [4], but since it ignores the channel/land effect, the gradient in gas channels, the in-plane transport, etc., the accuracy of these models is limited to smaller cells with high gas flow rates or low current densities.

3D PEMFC models directly consider the flow field designs, which enables them to capture the large heterogeneity across the CL surface and achieve higher precision. Yao et al. [16] developed a 3D PEMFC model with CL agglomerates and subsequently employed the model to train a neural network (NN) for designing the CLs, highlighting the volume fraction of ionomer as the most influential factor. However, to mitigate the computational cost, only a single gas channel was considered. Martín-Alcántara et al. [17] conducted a 3D PEMFC simulation, which also considered a single gas channel, and concluded that higher temperatures can lead to better performance due to the enhanced water transport in the membrane. García-Salaberri and Sánchez-Ramos [18] combined a 3D single channel continuum model with a modified pore-network model for liquid water saturation to investigate the channel-rib effect, and a lower GDL thermal conductivity was found to be beneficial for reducing saturation under the rib. However, these 3D models can have a significantly larger number of mesh elements in comparison with the 1D models, resulting in substantially higher computational cost. Consequently, many of these models only account for a single gas channel [16], while models with large active areas and multiple gas channels may encompass over ten million mesh elements and require several days for computation [19]. Additionally, large 3D models may also encounter numerical problems, leading to unstable convergence and solver failure [20].

To avoid the lengthy simulation time associated with the 3D models, a hierarchical 3D+1D method was devised by Cordiner et al. [21], where a 3D gas channel/gas diffusion layer (GDL) model is combined with a local electrochemical sub-model. Given that the thicknesses of the CLs/micro porous layers (MPLs)/membrane are around two to three magnitudes smaller than the length and width of these layers, the mass, heat, electron, and proton transport in these thin layers are governed by the transport in the thickness direction [19]. Thus, by neglecting the in-plane transport and simplifying the CLs/MPLs/membrane to lumped models or reduced order models, the hierarchical method enables the removal of mesh elements in those layers, resulting in a significant reduction in computational time. However, the simplifications made to these layers also lead to homogenized current density and transport properties along the thickness direction, thereby compromising model accuracy, especially under high current densities, low humidity, or low stoichiometry conditions. To date, various hierarchical models have been developed for PEMFCs. Grimm et al. [22] established a 2D+1D model that discretized the cell area into 2D segments with a local electrochemical sub-model. The model considered the anode recirculation loop, and its low computational cost facilitates the rapid optimization of water management. It was observed that flow fields allowing internal water circulation yielded benefits through a more uniform distribution of anode humidity. However, the additional assumptions required by this segmented method, such as linear pressure drop and ignoring condensation, may potentially result in an overestimation of performance under conditions of high humidity and high current density. Xie et al. [19] developed a hierarchical model where a linearized node-based 1D MPL/CL/membrane electrochemical model was coupled with a 3D model via an extra data exchange layer. The model was then used for the analysis of PEMFC performance under GDL deformation due to the assembly pressure [23] and investigating the internal transport under different flow field designs [24]. However, despite being significantly faster than whole 3D models, predictions of the 3D+1D model can diverge from those of the full 3D model by over 15% [19], possibly due to the ignored nonlinearity in the CLs and membrane [4].

In contrast to the above physics-based models, data-driven methods based on machine learning rely directly on the input-output relationship of the training data without delving into detailed mechanisms [25], but their accuracy is strongly dependent on the quantity and quality of the data [6]. In many studies, the experimental results are directly applied as the training data for the purpose of performance prediction [26], fault detection [27], remaining useful life estimation [28], etc. Yet, owing to the cost and time constraints associated with acquiring experimental data, these models usually limit their consideration to a specific set of operating conditions and design parameters, making them only applicable to certain working scenarios.

Due to these considerations, data-driven models trained with data generated by complex physics-based models have become increasingly popular [6]. These data-driven surrogate models are able to accurately capture the input-output relationship of the physics based-models with less than 1% computing cost, thereby enabling the broader application of continuum models [29]. Feng et al. [30], for instance, trained a NN with the data from a 1D PEMFC model, and the operating conditions of a fuel cell stack were optimized by the particle swarm optimization (PSO) algorithm to achieve maximum power density. Legala et al. [31] compared different machine learning methods based on a dataset generated from physics-based models, with NNs found to have higher accuracy, whereas support vector machines were advantageous when focusing on a single output. While the above models only considered steady-state conditions, methods like long short-term memory network (LSTM) are also applicable to dynamic scenarios. In the study of Wang et al. [32], three data-driven approaches, namely multivariate polynomial regression, support vector machine, and LSTM, were compared on a dynamic dataset synthesized with a transient electrochemical model. While all methods showed comparable accuracy in predicting cell voltage, LSTM notably outperformed the other two methods for the prediction of resistance.

To extend the generalizability of the surrogate models, some studies also used 3D models to generate training data. Based on a dataset of 85 simulation results generated by a 3D two-phase continuum model, Vaz et al. [33] compared a NN surrogate model with the response surface approximation (RSA) method. The root mean square error (RMSE) of the NN was found to be 50% smaller than that of the RSA. However, in a

similar comparison conducted by Wang et al. [34], the RSA was found to have higher accuracy with smaller datasets (46 points), but the advantage diminishes with increased dataset size (up to 114 sample points). In addition to the prediction of polarization curves, Wang et al. [35] developed a data-driven surrogate approach, which was used to capture the fuel cell performance as well as the contours of the physics fields predicted by a 3D physics-based model. However, challenges persist as the 3D models in these studies may require over 10 h to generate a single data point. Consequently, surrogate models are usually restricted to small cells, and can deviate from physics-based models by as much as 24% due to the scarcity of training data [35], indicating that a fast yet accurate 3D model is still required before the widespread adoption of these surrogate approaches.

To effectively capture the heterogeneity within the membrane electrode assembly (MEA) without increasing the computational costs, a machine learning driven 3D+1D hierarchical model for PEMFCs is presented in this study. The model combines a 3D model covering the GDLs and the gas channels with a NN surrogate sub-model. The NN is trained using a large synthetic dataset generated from a full 1D electrochemical sub-model of the MPLs/CLs/membrane to capture its input-output behavior, with an RMSE of less than 0.2%. The proposed model can predict fuel cell performance with a computational cost similar to that of conventional linearized 3D+0D hierarchical models, while resolving the heterogeneity in the membrane and CLs. The model is validated using experimental data under different operating conditions and is then used for analyzing the effects of different operating conditions and flow field designs.

2. Model development

2.1. Model overview

Fig. 1 shows an overview of the machine learning accelerated 3D+1D model. As shown in the figure, the 3D sub-model, which includes the mass, heat, and electron transport in the GDLs and gas channels, is coupled with a full 1D description of the MPLs, CLs, membrane, and CL agglomerates by exchanging the boundary fluxes and boundary values at the MPL/GDL interface. To reduce the computational cost, a NN is developed to replace the dense-mesh, multi-physics 1D sub-model for coupling with the 3D domain. Large synthetic datasets are generated using the 1D model for training the NNs, ensuring an accurate description of the fuel cell's internal states. The 3D sub-model provides the values of the dependent variables at the cathode/anode GDL/MPL interfaces as Dirichlet boundary conditions for the 1D domain, which act as the input of the NN. As the NN replicates the input-output relationship of the 1D electrochemical model, these inputs enable the NN to compute the corresponding fluxes, which are then fed back into the 3D model as boundary conditions at the GDL/MPL interface during each iteration step.

The model is solved in COMSOL Multiphysics 5.3, and the NNs are imported into COMSOL with a custom MATLAB code.

2.2. 3D channel/GDL sub-model

In the 3D sub-model, it is assumed that the cell operates at steady state, all gas flow is laminar, the GDLs are homogeneous and continuum porous media, and that there is uniform temperature and voltage in the bipolar plates (BPs). In addition, it is also assumed that the liquid water saturation in the gas channel is small and therefore can be ignored. While some studies suggested liquid water accumulated in the channels could play an important role [36,37], the validity of this assumption is confirmed by a mist-flow model from the literature [19,37], and the result is shown in Figure S1 in the N

N materials. The extremely low liquid water saturation in the gas channels in the simulated case could be attributed to the small cell area and a high gas flow rate.

The 3D sub-model solves the mass, heat, species, and electron transport in the GDLs and gas channels, which incorporates six PDEs as follows:

Electron conservation:

$$-\nabla\cdot(\sigma_{e^-}\nabla\phi_{e^-}) = 0 \tag{1}$$

Energy conservation:

$$\nabla\cdot\left(\varepsilon_p(1-s)\rho_g C_{p,g}\mathbf{u}_g T\right) - \nabla\cdot(k\nabla T) = S_T \tag{2}$$

Mass conservation:

$$\nabla\cdot\left(\rho_g\mathbf{u}_g\right) = S_m \tag{3}$$

Momentum conservation:

$$\frac{\rho_g\nabla\left(\mathbf{u}_g\mathbf{u}_g\right)}{\varepsilon_p^2(1-s)^2} = \nabla\left[-P_g + \frac{\mu_g\left(\nabla\mathbf{u}_g + \nabla\mathbf{u}_g^T\right)}{\varepsilon_p(1-s)} - \frac{2\mu_g\nabla\mathbf{u}_g}{3\varepsilon_p(1-s)}\right] - \left(\frac{\mu_g}{K_{eff}} + \frac{S_m}{\varepsilon_p^2(1-s)^2}\right)\mathbf{u}_g \tag{4}$$

Gaseous species conservation (i for H_2O, O_2, N_2, and H_2):

$$\nabla\left(\rho_g\mathbf{u}_g Y_i\right) - \nabla\left(\rho_g D_i^{eff}\nabla Y_i\right) = S_i M_i \tag{5}$$

Liquid water conservation:

$$-\nabla\cdot\left(\frac{\kappa}{\mu_w V_w}\nabla P_l\right) = S_{ec} \tag{6}$$

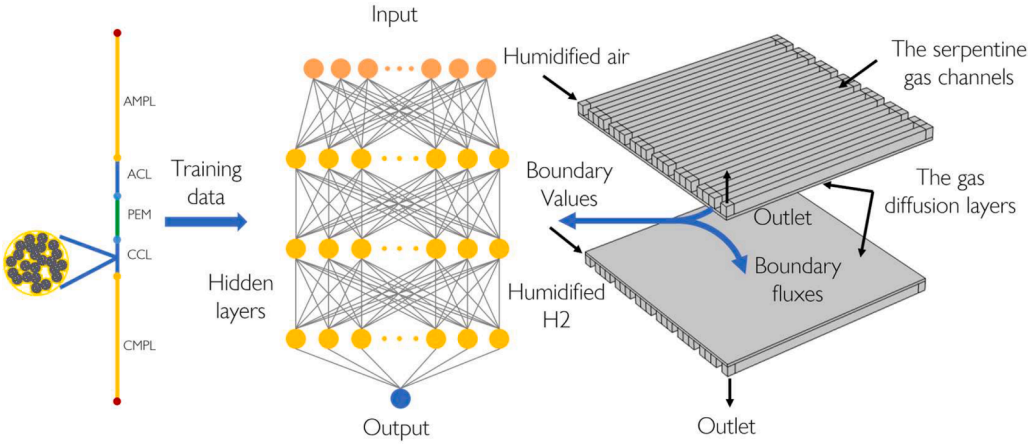

Fig. 1. Schematic illustration of the NN driven 3D+1D model, with the NN serving as a surrogate for the 1D sub-domain.

where σ_{e^-}, k, ρ_g, ε_p, s, μ_g, K_{eff}, D_i^{eff}, M_i, κ, μ_w, and V_w are the electric conductivity, the thermal conductivity, the gas density, the porosity, the liquid water saturation, the gas viscosity, the effective gas permeability, the effective gas diffusion coefficient, the molar mass of species i, the liquid water viscosity, and the liquid water molar volume, respectively. The source terms and the boundary conditions of these PDEs are shown in Table 1 and Table 2, respectively. While the electron and liquid water conservation equations are only solved for the GDLs, other equations are solved for both GDLs and gas channels. For all porous layers, the effective transport properties are used, which can be found in Table S1 in the supplementary materials. The geometric properties of the 3D sub-model are the same as the experiment and are listed in Table 3. The default segregated solver and relative tolerance from COMSOL Multiphysics were used for the 3D model, with some of the segregated steps modified to have a smaller initial damping factor and more iterations.

2.3. 1D membrane electrode assembly (MEA) sub-model

The physics-based 1D electrochemical model

The mass transport, heat transfer, and electrochemical reactions in the CLs and MPLs are first described by a 1D sub-model. This sub-model is based on the study of Vetter and Schumacher [12] and is similar to the 1D model used in our previous work [4]. The governing PDEs can be written as:

Electron conservation:

$$-\nabla\cdot(\sigma_{e^-}\nabla\phi_{e^-}) = S_{e^-} \tag{7}$$

Proton conservation:

$$-\nabla\cdot(\sigma_p\nabla\phi_p) = S_p \tag{8}$$

Energy conservation:

$$-\nabla\cdot(k\nabla T) = S_T \tag{9}$$

Gaseous species conservation ($i = H_2$, O_2 and H_2O(g)):

$$-\nabla\cdot\left(D_i^{eff}\frac{P}{RT}\nabla X_i\right) = S_i \tag{10}$$

Liquid water conservation:

$$-\nabla\cdot\left(\frac{\kappa}{\mu_w V_w}\nabla P_l\right) = S_s \tag{11}$$

Water conservation in the ionomer phase:

$$-\nabla\cdot\left(\frac{D_\lambda}{V_m}\nabla\lambda - \frac{\xi}{F}j_p\right) = S_\lambda \tag{12}$$

where σ_p, D_λ, ξ, j_p, and V_m are the proton conductivity, the water diffusion coefficient in ionomer phase, the electro-osmotic drag coefficient, the proton flux, and the molar volume of ionomer, respectively. The source terms and boundary conditions of these PDEs are summarized in Tables 4 and 5, respectively.

The hydrogen oxidation reaction (HOR) is described by the Butler-Volmer equation:

Table 1
Source terms of the 3D sub-model.

Source terms	Values
Heat	$S_T = \begin{cases} H_{ec}S_{ec} & \text{Channels} \\ H_{ec}S_{ec} + \sigma_{e^-}\lVert\nabla\phi_{e^-}\rVert^2 & \text{GDLs} \end{cases}$
Mass	$S_m = -S_{ec}M_{H_2O}$
H_2	0
H_2O	$S_{H_2O} = -S_{ec}$
O_2	0
Condensation/Evaporation	$S_{ec} = \begin{cases} \gamma_{ec}\varepsilon(1-s)(c_{H_2O}-c_{sat})c_{H_2O} > c_{sat} \\ \gamma_{ec}\varepsilon s(c_{H_2O}-c_{sat})c_{H_2O} < c_{sat} \end{cases}$

Table 2
Boundary conditions of the 3D sub-model.

Scalars	Boundary conditions	Boundary regions
ϕ_{e^-}	$\phi_{e^-} = 0$	Anode GDL/BP interface
	$\phi_{e^-} = U_{cell}$	Cathode GDL/BP interface
	$-\sigma_{e^-}\frac{\partial\phi_{e^-}}{\partial z} = j_{e^-,NN}$	GDL/MPL interfaces
T	$T = T_{cc}$	All outer surfaces
	$-k\frac{\partial T}{\partial z} = j_{T,NN}$	GDL/MPL interfaces
P_g	$P_g = P_o$	Anode/cathode outlets
u_g	$u_g = \frac{v_a}{H_{CH}W_{CH}}$	Anode inlet
	$u_g = \frac{v_c}{H_{CH}W_{CH}}$	Cathode inlet
Y_{O2}	$Y_{O_2} = \frac{0.21(1-RHX_{sat})M_{O_2}}{M_g}$	Cathode inlet
	$Y_{O_2} = 0$	Anode inlet
	$-D_{O_2}\frac{\partial c_{O_2}}{\partial z} = j_{O_2,NN}$	GDL/MPL interfaces
Y_{H2O}	$Y_{H_2O} = \frac{RH_aX_{sat}M_{H_2O}}{M_g}$	Anode inlet
	$Y_{H_2O} = \frac{RH_cX_{sat}M_{H_2O}}{M_g}$	Cathode inlet
	$-D_{H_2O}\frac{\partial c_{H_2O}}{\partial z} = j_{H_2O,NN}$	GDL/MPL interfaces
Y_{H2}	$-D_{H_2}\frac{\partial c_{H_2}}{\partial z} = j_{H_2,NN}$	GDL/MPL interfaces
P_l	$P_l = P_g$	GDL/channel interfaces
	$-\frac{\kappa}{\mu_w V_w}\frac{\partial P_l}{\partial z} = j_{l,NN}$	GDL/MPL interfaces

Table 3
Geometric properties of the 3D sub-model and design parameters for the 1D sub-model.

Property	Values
Channel width	0.80 mm
Channel height	1 mm
Channel length	22.36 mm
Land width	0.86 mm
Cell width	22.36 mm
Cell length	22.36 mm
GDL thickness (including MPL)	342 μm [38] (Value for W1S1010 GDL)
MPL thickness	45 [38] (Value for W1S1010 GDL)
Pt loading	0.5 mg cm^{-2}
Catalyst type	60 wt% Pt on Vulcan carbon
Ionomer/Carbon ratio	0.6
Electro chemical surface area (ECSA)	12.3 m^2 cm^{-3} (calculated with cyclic voltammetry data, equivalent to 24.6 m^2 g^{-1})

Table 4
Source terms of the 1D electrochemical model.

Source terms	Values
Electrons	$S_{e^-} = -i$CLs
Protons	$S_P = i$CLs
Heat	$S_T =$ $\sigma_{e^-}(\nabla\phi_{e^-})^2 + H_{ec}S_{ad}$MPLs; $\{\sigma_{e^-}(\nabla\phi_{e^-})^2 + \sigma_P(\nabla\phi_P)^2 + \left(i\eta - \frac{iT\Delta S}{2F}\right) + H_{ad}S_{ad} + H_{ec}S_{ad}$CLs; $\sigma_P(\nabla\phi_P)^2$Membrane
H_2	$S_{H_2} = -\frac{i}{2F}$anodeCL
H_2O	$S_{H_2O} = -S_{ec}$
O_2	$S_{O_2} = \frac{i}{4F}$cathodeCL
Dissolved water	$S_\lambda = \begin{cases} S_{ad} - \frac{i}{2F} & \text{cathodeCL} \\ S_{ad} & \text{anodeCL} \end{cases}$
Condensation/ Evaporation	$S_{ec} = \begin{cases} \gamma_{ec}\varepsilon(1-s)(c_{H_2O}-c_{sat})c_{H_2O} > c_{sat} \\ \gamma_{ec}\varepsilon s(c_{H_2O}-c_{sat})c_{H_2O} < c_{sat} \end{cases}$

Table 5
Boundary conditions of the 1D electrochemical model.

Scalars	Boundary conditions	Position
ϕ_{e^-}	Dirichlet boundary conditions from the 3D model	GDL/MPL interfaces
	Zero flux	CL/Membrane interfaces
ϕ_P	Zero flux	MPL/CL interfaces
λ	Zero flux	MPL/CL interfaces
T	Dirichlet boundary conditions from the 3D model	GDL/MPL interfaces
X_{O2}	Dirichlet boundary conditions from the 3D model	Cathode GDL/MPL interface
X_{H2O}	Dirichlet boundary conditions from the 3D model	GDL/MPL interfaces
P_l	Dirichlet boundary conditions from the 3D model	GDL/MPL interfaces

$$i = ai_{0,\mathrm{HOR}}\left[\exp\left(\frac{F}{RT}\eta_{\mathrm{HOR}}\right) - \exp\left(-\frac{F}{RT}\eta_{\mathrm{HOR}}\right)\right] \tag{13}$$

where a is the electrochemical surface area, $i_{0,\mathrm{HOR}}$ is the HOR exchange current density and η is the electrochemical overpotential, which can be calculated as:

$$\eta = \phi_{e^-} - \phi_P - U_0 \tag{14}$$

where U_0 is the reversible potential.

The oxygen reduction reaction (ORR) in the cathode CL is strongly dependent on the oxygen transport in the CL ionomer and is described by a Pt/C/ionomer agglomerate sub-model, and the model equations are listed in Table 6.

Cell design parameters like Pt loading are specified in Section 3. All other physicochemical properties and empirical equations are listed in Table S1 in the supplementary materials. The default solver and relative tolerance from COMSOL were used for the 1D model and data generation. This solver, however, encountered convergence issues under certain operating conditions, particularly when liquid water began to emerge. As an alternative, another segregated solver was also applied to these conditions, which partially resolved the numerical problem but still failed at a few data points.

NN surrogate model

The NN, delineating the mapping relationship between the input vector and output vector, comprises of an input layer, three hidden layers with 20 neurons per layer, and an output layer. The hidden layers perform a nonlinear transformation for feature extraction, while the output layer gives a linear combination of output weights. The size of the NN is determined by balancing computational efficiency and accuracy. The initial configuration involved a single hidden layer, and the number of hidden layers was progressively increased until an acceptable level of error was achieved on the test data. Increasing the number of hidden layers from one to three resulted in a reduction of the RMSE and max error of current prediction from 1.6% and 24% to 0.17% and 2.45%, respectively. Additional hidden layers led to only minor improvements while significantly increasing the training time. As outlined in Table 5, the 1D domain employs values such as temperature, relative humidity (RH), and O_2 molar fraction as the boundary conditions. These boundary conditions also serve as the input parameters of the NNs, which are detailed in Table 7 along with their corresponding maximum/minimum values. Note that while some of the inputs are restricted to relatively narrow ranges close to the experiments to enhance accuracy, these ranges can be easily extended to a wider spectrum of operating conditions. The NNs provide the boundary fluxes on the MPL/GDL interfaces for the 3D domain, which include the local current output, anode/cathode water fluxes in liquid/vapor forms, and anode/cathode heat fluxes. The H_2 and O_2 fluxes at the interface can then be calculated based on the current densities:

$$\begin{cases} j_{H_2} = \dfrac{j_{e^-}}{2F} \\ j_{O_2} = -\dfrac{j_{e^-}}{4F} \end{cases} \tag{15}$$

For simplicity, each NN only generates one output, and a total of seven NNs are used as the surrogate sub-model. Additional NNs are also used to extract the internal properties from the 1D domain, but these NNs do not influence the result of the 3D model.

A large synthetic dataset generated by the 1D electrochemical model is used to train the NNs. As artificial NNs are optimal for interpolation instead of extrapolation, the ranges of the input variable are intentionally broader than the typical conditions given by the 3D domain. The dataset is initiated with the generation of data using the electrochemical model with the boundary values (maximum/minimum values), resulting in 10,240 data points, but the solver consistently encounters convergence issues at some data points where liquid water begins to emerge. Subsequently, additional data points are generated randomly following the uniform distribution within the boundary values defined in Table 7, with 74,200 data points synthesized from 1D electrochemical model. The GDLs were removed from the 1D model when generating the data as they are considered in the 3D domain.

To enhance network convergence performance, a normalization of the input/output data with different magnitudes is essential, which in this work is achieved using the max-min method. Mean squared errors (MSE) between the prediction and fluxes generated by the 1D electrochemical model are used as the cost evaluation function. The synthetic data points are randomly divided into a training set and a testing set at an 8:2 ratio. The Bayesian regularization back-propagation method is employed to train the NNs until reaching 1000 epochs or achieving an MSE less than 10^{-6}.

Table 6
Equations of the agglomerate sub-model [4,39].

	Expressions
Thiele modulus	$\beta = \dfrac{d_{\mathrm{agg}}}{6}\sqrt{\dfrac{q_C}{D^{\mathrm{eff}}_{O_2,\mathrm{agg}}}}$
Agglomerate effective factor	$Er = \dfrac{1}{\beta}\left(\dfrac{1}{\tanh(3\beta)} - \dfrac{1}{3\beta}\right)$
Cathode half-cell reaction coefficient	$q_C = \dfrac{ai_{0,c}(1-\theta_{\mathrm{PtO}})}{4F(1-\varepsilon_p)c^{\mathrm{ref}}_{O_2}}\left[\exp\left(\dfrac{F}{RT}\eta\right) - \exp\left(-\dfrac{F}{RT}\eta\right)\right]$
Cathode catalyst layer current density	$i = 4F\dfrac{P_{O_2}}{h_{O_2}}\left[\dfrac{1}{q_C Er(1-\varepsilon_p)} + \dfrac{(d_{\mathrm{agg}}+2\delta_{\mathrm{agg}})\delta_{\mathrm{agg}}}{(1-s)a_{\mathrm{agg}}d_{\mathrm{agg}}D_{O_2,\mathrm{flim}}}\right]^{-1}$
Platinum oxide formation	$(1-\theta_{\mathrm{PtO}})\exp\left(\dfrac{F}{2RT}\eta_{\mathrm{PtO}} - \dfrac{10\mathrm{kJ/mol}}{RT}\theta_{\mathrm{PtO}}\right) - \theta_{\mathrm{PtO}}\exp\left(-\dfrac{F}{2RT}\eta_{\mathrm{PtO}}\right) = 0$
Overpotential of PtO formation, η_{PtO} (V)	$\eta_{\mathrm{PtO}} = \phi_{e^-} - \phi_P - 0.81\mathrm{V}$

3. Experimental

The 5-layer fuel cell MEAs bought from FuelCellStore were used as

Table 7
Ranges of the input parameters for the NNs.

Input boundary values	Minimum value	Maximum value
Anode temperature (°C)	70	90
Cathode temperature (°C)	70	90
Anode pressure (bar)	2.4	3
Cathode pressure (bar)	2.4	3
Anode capillary pressure (Pa)	0	1500
Cathode capillary pressure (Pa)	0	2000
Anode humidity	0.3	1.5
Cathode humidity	0.3	1.5
O_2 molar fraction in dry air	0.01	0.21
Voltage (V)	0	0.9

obtained. The MEAs comprised of N212 membranes, and the 5 cm^2 active area cathode and anode comprised of W1S1010 GDLs with embedded MPLs and 0.5 mg cm^{-2} 60 wt% Pt on Vulcan carbon, with an I/C ratio of 0.6. The single cell fuel cell was assembled using Scribner hardware comprising of graphite serpentine channel flow fields on both cathode and anode. The MEA was also gasketed with PTFE sheets on both sides to achieve 20% compression of GDLs. The cell was assembled at 552 kPa final pressure in a star pattern at 138, 276, 414 and 552 kPa steps, and then connected to a Scribner Fuel Cell Test Station (850e) equipped with impedance analyzer (885-HS), heated cuffs and back-pressure unit. The stoichiometry for the cathode and anode was 2.50 and 1.25, respectively, with a minimum cathode/anode flow rate of 0.5 L min^{-1} air and 0.25 L min^{-1} H_2. The fuel cell was allowed to equilibrate at 70 °C for an hour and was then connected to the potentiostat. To generate fuel cell polarization curves, the cell was held at each potential from open circuit to 0.05 V at 50 mV intervals for at least 3 mins. At higher current densities, the hold was extended such that stable current was generated for at least 3 min, and the average current density for the last 30 s at each potential was recorded.

As summarized in Table 8, the outlet pressure and cell temperature were kept at 250 kPa and 80 °C, respectively, and the RH varied from 40% to 100%, highlighted in bold. After each RH change, the cell was equilibrated for 1 h prior to measurement. The high frequency resistance (HFR) at each voltage and RH was recorded and the electrochemical surface area (ECSA) of the catalyst layers was calculated with cyclic voltammetry. Impedance measurements were also recorded between 200 kHz and 100 mHz while the fuel cell was operating under the selected conditions at 0.9 V using an external Biologic Potentiostat (VSP-3e) equipped with a 20A/20 V booster (VMP3B-20).

4. Results and discussion

4.1. Validation of the NN surrogate sub-model

The accuracy of the trained NNs is evaluated with the test data, with the normalized error of the fluxes displayed in Fig. 2a-g. The normalized RMSE and maximum errors are also listed in Table 9, with RMSE and max error less than 0.17% and 3%, respectively. For clarity, a comparison of the predicted polarization curves of the 1D electrochemical model and the NN surrogate model under four operating conditions extracted from the 3D sub-model under 40% to 100% RH is illustrated in Fig. 2h, which also shows an excellent agreement. Details of these four operating conditions can be found in Table S2 in the supplementary materials.

4.2. Validation of the NN driven 3D+1D model

The proposed model is validated to the experimental data conducted under four different RH conditions, with detailed information available in Table 7. Both the polarization curves and the HFR are subjected to verification. As depicted in Fig. 3a, the simulation closely aligns with the experimental polarization curves. The model captures both the significant performance variations at the low current density region and the transition into mass transport limitation at higher current densities. The performance of the fuel cell exhibits improvement with increasing RH, but RH levels above 80% lead to reduced limiting current density due to the lowered air fraction and hindered oxygen transport caused by liquid water. At 40% RH, minor overestimations of limiting current and voltage loss at moderate current densities can be observed, which could be explained by the predicted HFR. Further elaboration on this will be provided in subsequent paragraphs.

Table 8
Operating conditions of the experiments, with the difference in RH highlighted in bold.

Conditions	Temperature	Inlet RH	Outlet Pressure	Inlet flow rate
1	353 K	**100%**	250 kPa	0.5 L min^{-1} (cathode) 0.25 L min^{-1} (anode)
2	353 K	**80%**	250 kPa	0.5 L min^{-1} (cathode) 0.25 L min^{-1} (anode)
3	353 K	**60%**	250 kPa	0.5 L min^{-1} (cathode) 0.25 L min^{-1} (anode)
4	353 K	**40%**	250 kPa	0.5 L min^{-1} (cathode) 0.25 L min^{-1} (anode)

A steady-state model is used in this study as the NN surrogate model lacks the time-dependent properties of the full-1D model, thus it is not feasible for the model to directly perform frequency and impedance analysis. Utilizing the transmission line expression of a fuel cell with negligible electric resistance in the catalyst layer [40], both the charge-transfer resistance and the proton resistance in the ionomer are effectively short-circuited by the double-layer capacitance at high frequency. As a result, the HFR from the model can be calculated by summing the average membrane resistance and the electrical resistance of the MPLs and GDLs.

A comparison between the model and the experimental data is shown in Fig. 3b, revealing good agreement between the simulated HFR and HFR values from the experiments, especially for higher RHs. Under low RH, the HFR is overestimated at moderate current densities, resulting in a lower cell potential as depicted in Fig. 3a. The discrepancy may suggest either an underestimated membrane water diffusion coefficient, an overestimated water vapor transport, or an overestimated membrane water desorption. In addition, the trend of increasing HFR at 40% RH at voltage values below 0.2 V is not captured by the model, which might be due to the uncertainty in membrane properties like the electro-osmotic drag coefficient and/or water diffusion coefficient in the ionomer, and this continuous decrease of HFR in the simulation resulted in a higher limiting current density comparing to experimental observations. It should be noted that the simplifications inherent in the 1D electrochemical model could also contribute to such discrepancies. As the proposed NN acceleration approach is a generalized method for all hierarchical models, these assumptions can be potentially replaced with more detailed mechanisms such as chemical potential-based membrane transport model or incorporating multi-step oxygen reduction reactions to enhance accuracy. These enhancements are outside the current scope of our work and remain avenues for future research.

To assess the computational efficiency of the proposed modeling framework, the computing time of the NN driven 3D+1D model is compared with a 3D+0D model where the MPLs, CLs, and membrane are described with a lumped empirical equation, which is detailed in the supplementary materials. The results in Table 10 show that the 3D+0D model has similar computational time compared to the proposed NN driven 3D+1D model under 100% RH. However, the 3D+0D model suffers from convergence issues when a liquid water boundary exists due to the undersaturated gas near the inlet, which leads to the significantly longer computational time at 80% RH, a trend that is also observed in the 1D electrochemical model. At 40% RH, the difference becomes much smaller, as liquid water only begins to form when approaching limiting currents. Thus, it can be inferred that while retaining the nonlinearity of the 1D domain, the computing time of the NN driven 3D+1D model remains comparable to a hierarchical model with lumped electrochemical sub-model.

Table 10 also reveals that the NN surrogate model exhibits negligible computational time compared to the 1D electrochemical model, which suggests that the NN driven 3D+1D model can be significantly faster comparing to a full 3D model. However, it should be noted that this advantage may diminish when only a single simulation is conducted, as the data generation and training of the NN also require time. Similar to the 3D+0D model, the 1D electrochemical model exhibits much longer computing time at 80% RH, indicating potential convergence issues when liquid water starts to be present in the cathode CL, which is also avoided by the NN surrogate model.

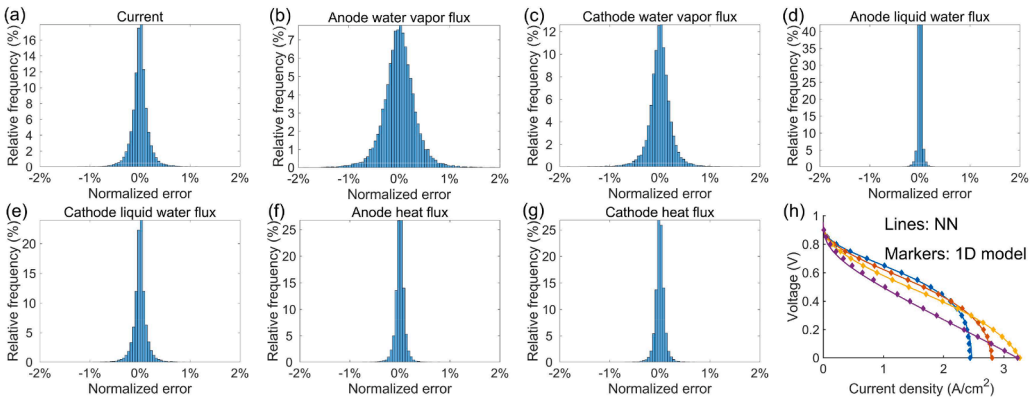

Fig. 2. Normalized errors of the NN surrogate sub-model and a comparison between the simulated polarization curves of the NN and the 1D electrochemical model. (a) Current density; (b) anode water vapor flux; (c) cathode water vapor flux; (d) anode liquid water flux; (e) cathode liquid water flux; (f) anode heat flux; (g) cathode heat flux; (h) polarization curves of the NN and the 1D electrochemical model under different operating conditions which are detailed in Table S2.

Table 9
Testing errors of the trained NNs.

Output boundary fluxes	RMSE (%)	Max error (%)
Current	0.17	2.45
Anode water vapor flux	0.07	1.14
Cathode water vapor flux	0.11	1.41
Anode liquid water flux	0.04	1.31
Cathode liquid water flux	0.11	2.58
Anode heat flux	0.05	0.85
Cathode heat flux	0.06	1.59

4.3. *Effect of operating conditions and flow field designs*

The above results have demonstrated that the operating conditions, such as RH, can have significant impact on the performance of PEMFCs. The proposed machine learning accelerated 3D + 1D model enables us to comprehensively investigate the influence of both operating conditions and flow field designs. In this section, the experimental operating conditions under 60% RH are used as the baseline condition, and further simulations are conducted for different stoichiometries and channel/land ratios. Detailed information of the four conditions to be analyzed can be found in Table 11, and the differences are highlighted in bold.

The simulated polarization curves, power densities, and HFR under these conditions are presented in Fig. 4. As depicted in Fig. 4a, the fuel cell achieves the highest efficiency and maximum power density under the fully humidified condition. The relatively small limiting current observed under such condition is attributed to the lower inlet oxygen concentration and increased oxygen transport resistance due to accumulated liquid water, indicating that the performance enhancement is primarily due to improved hydration of the membrane, which is

Table 10
Computing time of the NN driven 3D+1D model, 3D model without NNs, 1D electrochemical model, and NN surrogate model.

Operating conditions	Computing time per voltage point (s)			
	NN driven 3D+1D model	3D+0D model	1D electrochemical model	NNs
40% RH	363	356	0.8	0.0041
60% RH	372	470	0.7	0.0038
80% RH	343	498	1.2	0.0042
100% RH	335	333	0.7	0.0040
Hardware	Intel(R) Xeon(R) Silver 4110			

Table 11
Operating conditions and flow field designs for the simulation, with difference highlighted in bold.

Conditions	Baseline condition	Fully humidified	Moderate gas flow rate	High channel to land ratio
Temperature	353 K	353 K	353 K	353 K
RH	60%	**100%**	60%	60%
Outlet pressure	250 kPa	250 kPa	250 kPa	250 kPa
Anode flow rate	0.25 L min^{-1}	0.25 L min^{-1}	**1.25 stoichiometry**	0.25 L min^{-1}
Cathode flow rate	0.5 L min^{-1}	0.5 L min^{-1}	**2.5 stoichiometry**	0.5 L min^{-1}
Channel to land ratio	0.94	0.94	0.94	**2**

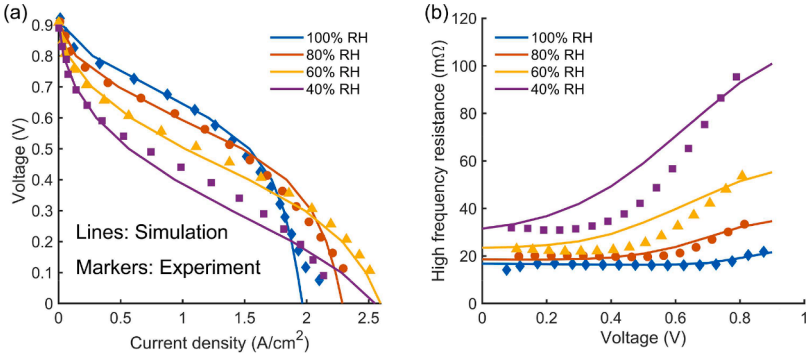

Fig. 3. Comparison between the experimental data and the simulation results of the NN driven 3D+1D model under four different inlet relative humidities. (a) Polarization curves; (b) HFR.

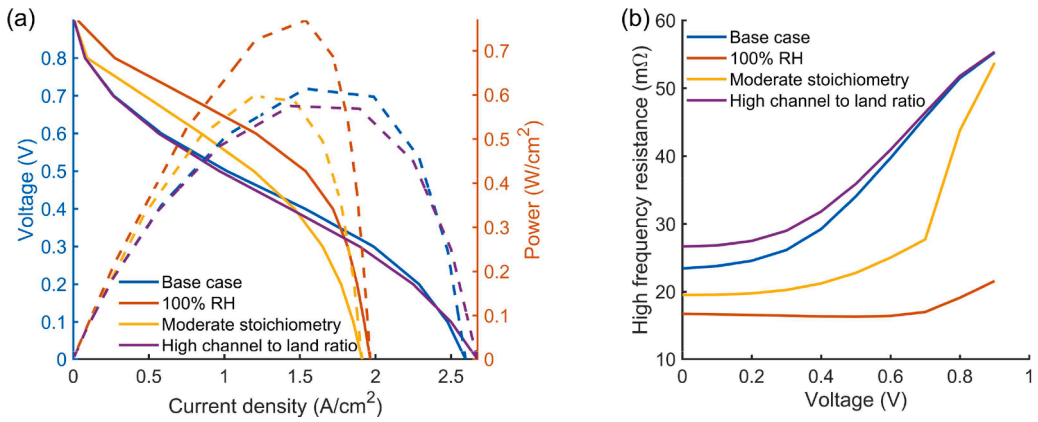

Fig. 4. Comparison between the simulated polarization curves, power densities, and HFR under the four different cases. (a) polarization curves and power densities; (b) HFR.

associated with significantly lower resistance, as displayed in Fig. 4b.

Under moderate stoichiometry, the reduction in oxygen supply results in the lowest limiting current. However, the decreased gas flow rate also promotes self-humidification due to the water generated by the electrochemical reaction, leading to a lower HFR and improved overall performance. The conflict between oxygen supply and self-humidification suggests that an optimal gas flow rate might exist when the fuel cell is not fully humidified. Conversely, a higher channel to land ratio enhances the oxygen transport but also facilitates the removal of the generated water. Despite having the highest limiting current under this case, this configuration exhibits slightly lower efficiency and power due to a higher HFR, as illustrated in Fig. 4b. Nonetheless, the impact of channel design on performance is relatively minor due to the high gas flow rate.

The significant influence of stoichiometry indicates the crucial role that the local distribution of oxygen, water, and current density can play in fuel cell performance. Fig. 5 illustrates the cathode local current density and the oxygen distribution at the GDL/MPL interface at 0.6 V. Despite the high gas flow rate, Fig. 5a reveals a substantial gradient in local current density within the cathode CL, with the outlet exhibiting nearly 50% higher current density than the inlet. From Fig. 5b and Fig. 5d, it can be observed that under the fully humidified condition, the oxygen concentration near the outlet is approximately 30% lower than in the baseline condition, resulting in significantly higher current density near the inlet, which is presented in Fig. 5c.

At lower gas flow rates, performance is constrained by both humidification and oxygen concentration. As depicted in Fig. 5f, the oxygen concentration near the outlet is over 50% lower than in Fig. 5b, resulting in a highest local current density in the middle of the cell, and a noticeable channel and land difference can be observed, as shown in Fig. 5e. Comparing Fig. 5h to Fig. 5b, it is evident that the high channel/land ratio reduces differences of the oxygen concentration between channels and lands. However, as oxygen is not the limiting factor at 0.6 V due to the high gas flow rate, the local current density profile in Fig. 5g remains very similar to the baseline condition.

The interplay between membrane resistance and oxygen oxidation reaction is further elucidated in Fig. 6, where voltage loss attributed to cathode reaction and membrane resistance is delineated in Fig. 6(a, c, e, g) and Fig. 6(b, d, f, h), respectively. As shown in Fig. 6a and Fig. 6b, both electrochemical and membrane voltage loss exhibit a relatively uniform distribution for the baseline condition, with a difference of approximately 50 mV and 10 mV, respectively. However, noting that the outlet has significantly higher current density, it can be inferred that the outlet has much smaller membrane resistance. As sufficient oxygen is supplied to the cathode CL, the exponential relationship between electrochemical overpotential and reaction rate minimizes the impact of the current density gradient on the reaction voltage loss. Under the fully humidified condition, however, the membrane potential loss is considerably smaller near the outlet due to the lower local current density. Meanwhile, oxygen transport limitations result in a much larger electrochemical overpotential near the outlet, as shown in Fig. 6d and Fig. 6c. A similar trend is observed for the moderate stoichiometry condition, but with a more pronounced difference due to a larger oxygen concentration gradient and the decreasing membrane resistance from inlet to outlet caused by self-humidification. Due to the high gas flow rate, the high channel/land ratio condition shows no observable difference compared to the baseline condition. In Fig. 6, it is also noticeable that the fuel cell displays a slightly higher membrane potential drop near the edges, with a difference of around 5 to 10 mV. This observation could be attributed to the connection between the current collector and the edges of the GDLs, which results in a smaller potential drop due to the electrical resistance in GDLs.

These distributions also undergo changes with varying loads on the fuel cell. As illustrated in Fig. 7, the highest local current density gradually transitions from outlet to inlet with increasing load under the 60% RH condition. This shift is attributed to the oxygen transport becoming the limiting factor with increasing gradient in oxygen concentration and decreasing HFR. Moreover, the gradient of the local current density intensifies with increased load, with the inlet exhibiting more than 2 times larger current output compared to the outlet at 0 V.

As the NN serves as a surrogate of a full 1D model, it can also elucidate the distribution of internal states across the thickness of the CLs and the membrane. Fig. 8a shows the distribution of hydrogen oxidation reaction in the anode CL under the baseline condition. Due to the rapid reaction kinetics, the reaction predominantly occurs near the anode CL/membrane interface, with 20% of the anode CL generates more than 99% of the current, especially near the inlet. Consequently, the proton flux in the anode CL is nearly zero before approaching the membrane, resulting in a minor electrolyte potential drop, as illustrated in Fig. 8b. In addition, as the majority of the anode CL contributes minimally to the overall current, it is reasonable to infer that reducing the anode CL thickness could effectively lower the Pt loading without compromising performance.

In contrast, the oxygen reduction reaction has sluggish kinetics, leading to a more uniform distribution, as shown in Fig. 8c. This results in a significantly larger potential drop in the cathode ionomer. Combined with the membrane resistance, the inlet electrolyte potential drop exceeds 0.7 V as the cell voltage approaches zero, which is the limiting factor for the local current output. The large ionomer resistance in the cathode CL agrees with the straight line observed in the mid to high frequency region [40] of our EIS data shown Fig. S4 and is likely due to the low I/C ratio. Conversely, the electrolyte potential drop is considerably smaller near the outlet, suggesting that the lower reaction rate near the outlet is likely due to the oxygen transport limitation. As a

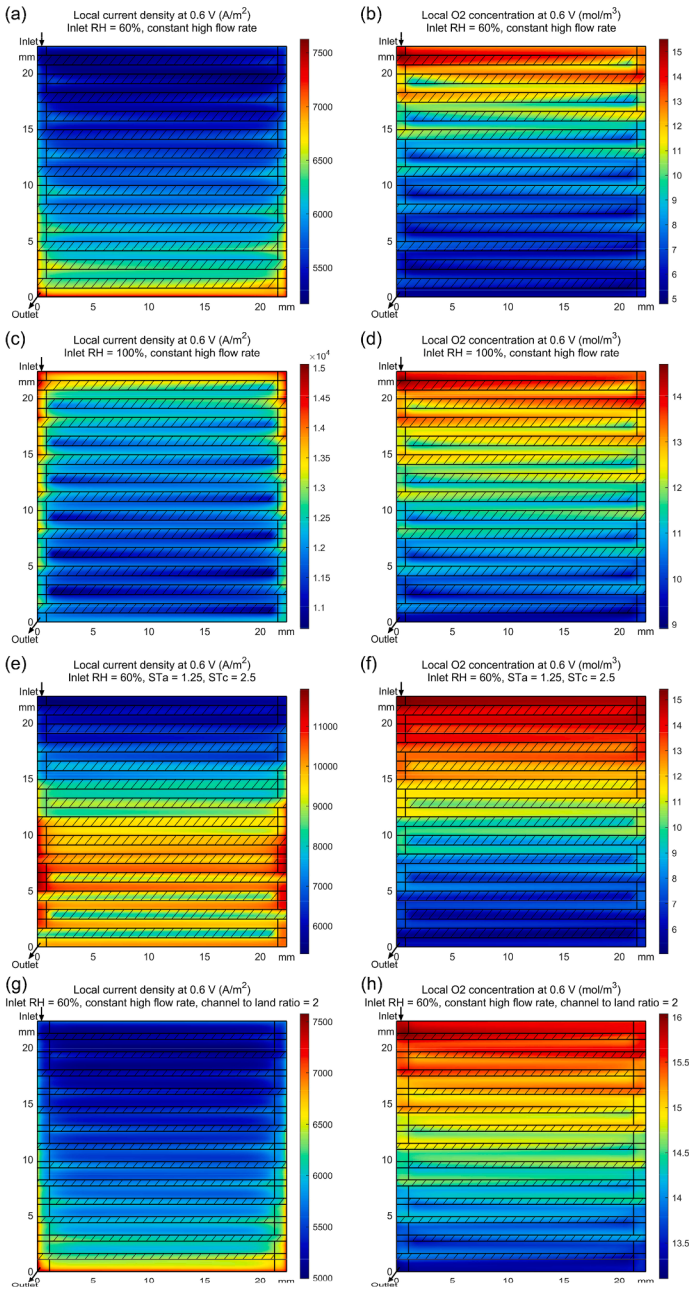

Fig. 5. Local distribution of current density in the cathode catalyst layer (a, c, e, g) and oxygen concentration at the cathode GDL/MPL interface (b, d, g, h). (a, b) baseline condition; (c, d) fully humidified condition; (e, f) moderate stoichiometry condition; (g, h) high channel to land ratio condition. The shaded area represents the regions beneath the land.

result, while the inlet exhibits a much larger oxygen reduction reaction rate on the membrane side due to the local electrochemical overpotential, the outlet's local oxygen concentration restricts the reaction rate near the membrane when the cell voltage is below 0.3 V. Similar trends can also be observed under the fully humidified condition, as depicted in Fig. 8d. However, owing to a lower oxygen concentration and a smaller effective diffusion coefficient caused by liquid water, oxygen transport also becomes the limiting factor for the inlet, and the outlet current density remains constant when reducing the cell voltage from 0.3 V to 0 V indicating that oxygen is depleted at the catalyst surface. The results shown in Fig 8 indicate that the strong nonlinear distribution along the thickness direction should not be ignored when using a hierarchical modeling approach.

As discussed previously, higher gas flow rate does not always enhance fuel cell performance. Following the testing protocol designed by the US department of energy [41] and the single cell test proposed by the Joint Research centre of the European Commission [42], we select the voltage at 0.8 A cm^{-2} as the performance index for optimization.

As shown in Fig. 9a, when the fuel cell is not fully humidified, the cell voltage at 0.8 A cm-2 decreases gradually with increasing anode stoichiometry. As hydrogen transport is not the limiting factor for fuel cell performance, a lower anode gas flow rate allows for the accumulation of water vapor, thereby leading to a better humidified membrane. At 100% RH, however, membrane hydration is no longer a limiting factor, thus variations in anode flow rate have minimal impact on fuel cell performance. In addition, it is noteworthy that when the fuel stoichiometry approaches 1, local hydrogen starvation can occur, which may result in carbon corrosion and durability issues [43].

Conversely, at 40% and 60% RH, higher cathode stoichiometry initially improves fuel cell performance, as shown in Fig. 9b. At 60% RH,

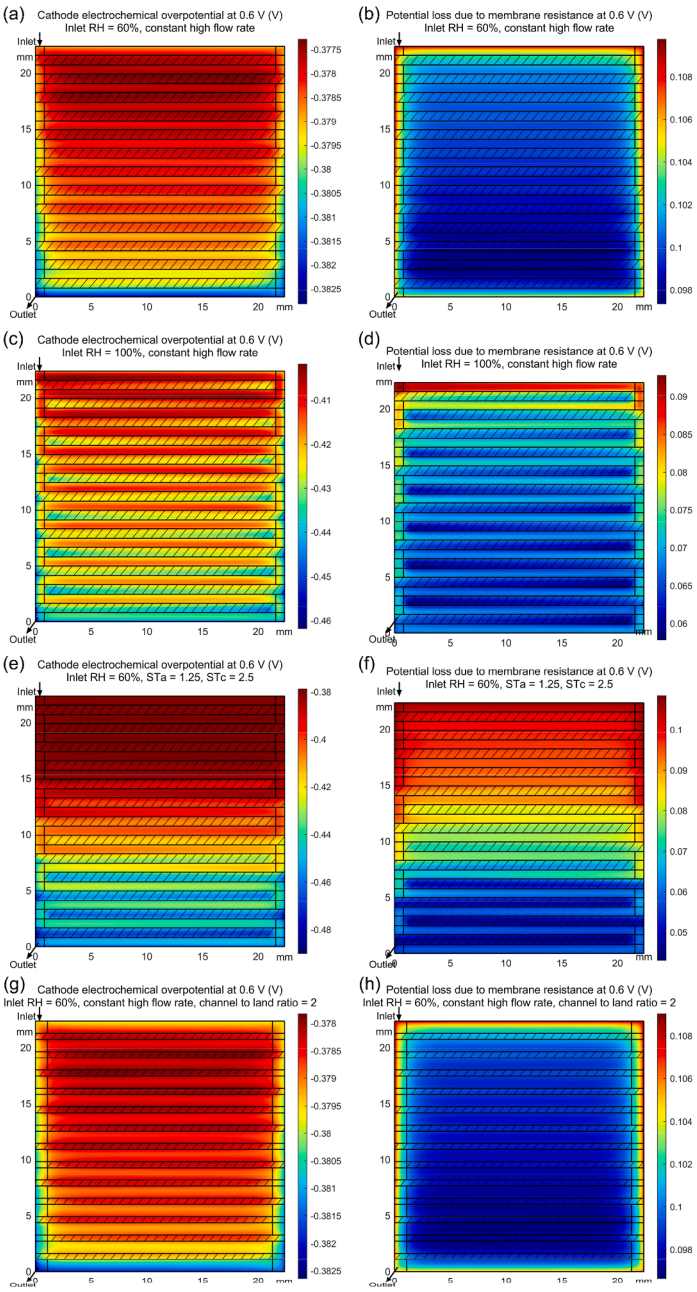

Fig. 6. Local distribution of cathode electrochemical overpotential (a, c, e, g) and potential loss due to membrane resistance (b, d, g, h). (a, b) baseline condition; (c, d) fully humidified condition; (e, f) moderate stoichiometry condition; (g, h) high channel to land ratio condition. The shaded area represents the regions beneath the land.

the voltage at 0.8 A cm^{-2} rises swiftly from a cathode stoichiometry of 1.5 to 3, peaking at 4.1. Beyond this point, the effect of oxygen transport limitation is countered by the hydration of the membrane. Further increases in cathode flow rate hinder self-humidification, slightly diminishing fuel cell performance. Since cathode stoichiometry above 3 has minimal impact on performance while increasing the energy consumption of gas pumps, the optimal range at 60% RH is likely 2.5 to 3. At 40% RH, performance peaks at a lower stoichiometry of 2.5 due to worse membrane hydration. At 80% and 100% RH, oxygen transport becomes the limiting factor rather than membrane resistance, thus increasing cathode stoichiometry up to 6 is still beneficial for fuel cell performance.

5. Conclusions

In this study, we introduce an approach utilizing neural network acceleration in a 3D+1D hierarchical model, which accounts for the nonlinearity along the thickness direction in catalyst layers, membrane, and microporous layers while maintaining a similar computing cost to conventional hierarchical methods. To address the limitations of the homogenized assumption in the 1D domain in conventional methods, this study integrates a 3D flow field with a neural network which acts as the surrogate for a full two-phase non-isothermal 1D electrochemical sub-model. The neural network uses the boundary conditions as input and is computed at every mesh grid at the gas diffusion layer/microporous layer interface to provide boundary fluxes for the 3D domain. Validations with experiment across a range of relative humidity values demonstrate the model's reasonable accuracy in predicting both polarization curves and high frequency resistance. Given that the neural network requires only 0.5% of the computing cost of a 1D electrochemical model, the proposed neural network driven 3D+1D model

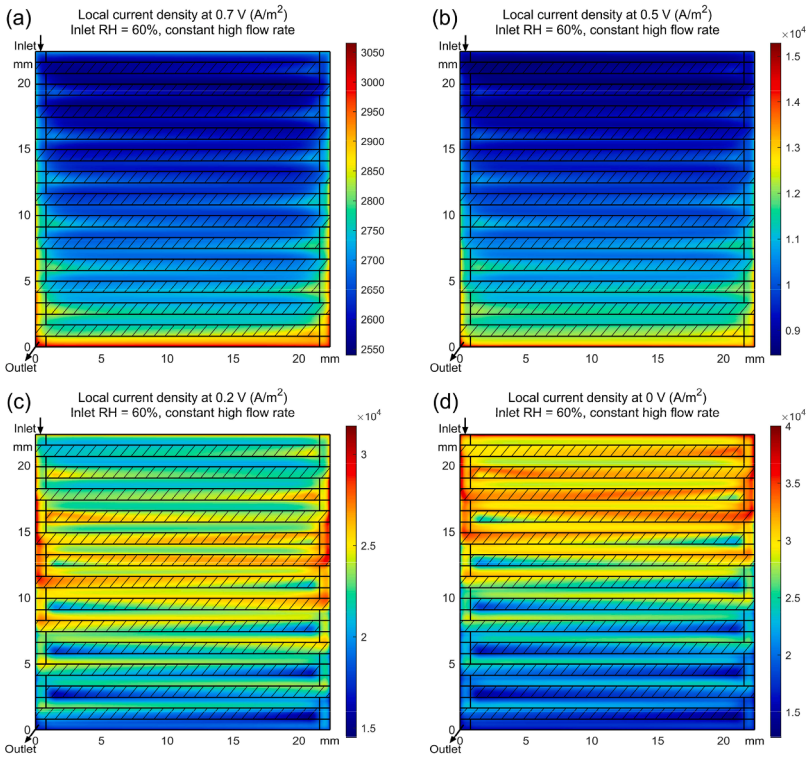

Fig. 7. Local current density at different voltages under the baseline condition. (a) 0.7 V; (b) 0.5 V; (c) 0.2 V; (d) 0 V. The shaded area represents the regions beneath the land.

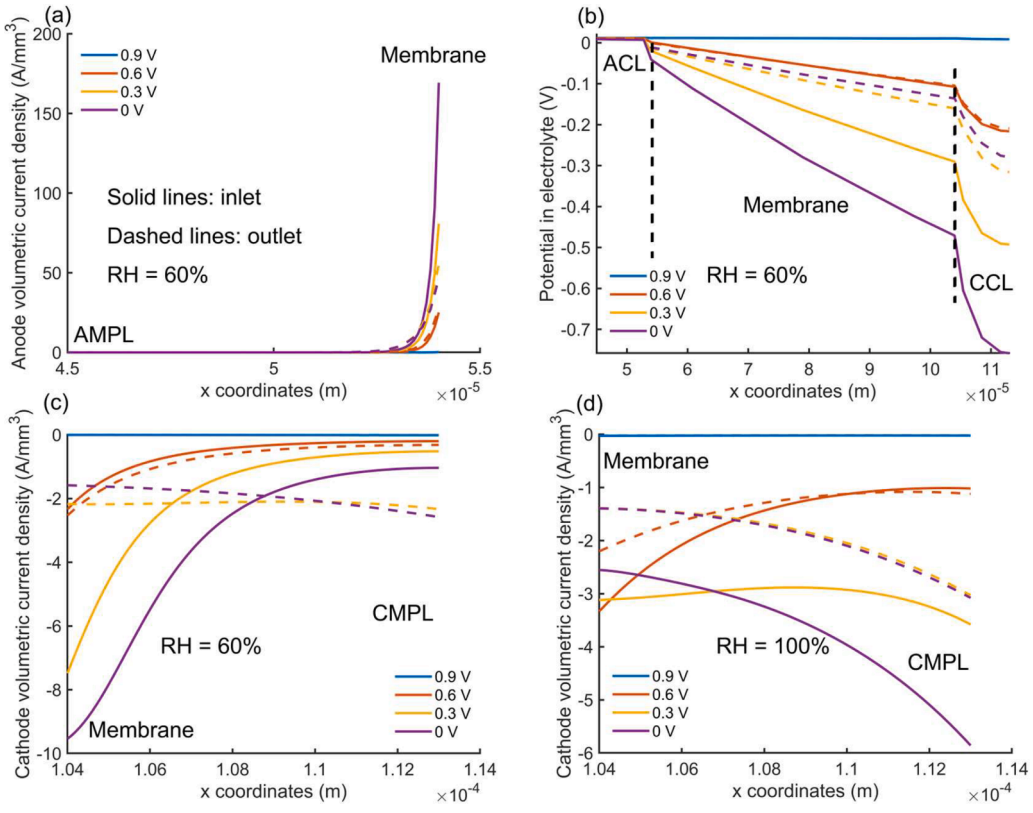

Fig. 8. Distributions of scalars in membrane and CLs along the thickness direction. (a) electrochemical current density of anode CL under the baseline condition; (b) potential in electrolyte phase under the baseline condition; (c) electrochemical current density of cathode CL under the baseline condition; (d) electrochemical current density of cathode CL under the fully humidified condition. Solid lines denote the inlet, while dashed lines represent the outlet.

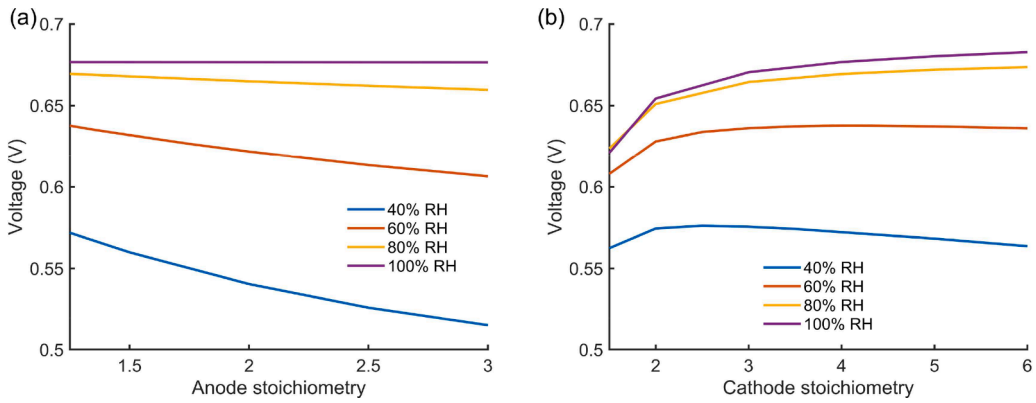

Fig. 9. Voltage at 0.8 A cm^{-2} with varying stoichiometry: (a) anode stoichiometry with varying RH and 4.1 cathode stoichiometry; (b) cathode stoichiometry with varying RH and 1.25 anode stoichiometry.

demonstrates computational speeds akin to those of a linearized 3D+0D model, which integrates a lumped electrochemical sub-model, while preserving the nonlinear distribution within the microporous layers, catalyst layers, and membrane.

Subsequent simulations explore the effects of operating conditions and gas channel designs. Results reveal that the performance of the fuel cell is enhanced at higher level of relative humidity, accompanied by a reduction in limiting current. Additionally, when the fuel cell is not fully humidified, the gas flow rate needs to be optimized to balance the oxygen transport and the hydration of the membrane. Detailed analysis of the 2D internal states distribution at the microporous layer/catalyst layer interface reveals that the observed performance variations are governed by the interplay between the electrolyte resistance and the oxygen reduction reaction, and the contribution of these factors evolves with changes in operating conditions, flow field designs, and the location within the fuel cell. More than 80% of the anode catalyst layer is found to generate less than 1% of the current, especially near the inlet, suggesting that the anode thickness can be reduced significantly to diminish the platinum loading. The pronounced nonlinearity of the current and potential distribution within the catalyst layers highlighted by the neural network result also indicates the inadequacy of the homogenized assumption used in the 1D domain of conventional 3D+1D models, which may compromise model accuracy.

CRediT authorship contribution statement

Yuwei Pan: Writing – original draft, Validation, Software, Methodology, Investigation, Conceptualization. **Haijun Ruan:** Writing – review & editing, Software, Methodology, Investigation, Conceptualization. **Billy Wu:** Writing – review & editing, Supervision. **Yagya N. Regmi:** Writing – review & editing, Validation, Supervision, Funding acquisition. **Huizhi Wang:** Writing – review & editing, Supervision, Funding acquisition. **Nigel P. Brandon:** Writing – review & editing, Supervision.

Declaration of competing interest

The authors declare the following financial interests/personal relationships which may be considered as potential competing interests: Yagya N. Regmi and Huizhi Wang reports financial support was provided by Engineering and Physical Sciences Research Council. If there are other authors, they declare that they have no known competing financial interests or personal relationships that could have appeared to influence the work reported in this paper.

Data availability

Data will be made available on request.

Acknowledgements

We wish to acknowledge the support of the Henry Royce Institute for advanced materials through the Materials Challenge Accelerator Programme (MCAP) funded from a grant provided by the Engineering and Physical Sciences Research Council (EP/X527257/1).

Supplementary materials

Supplementary material associated with this article can be found, in the online version, at doi:10.1016/j.egyai.2024.100397.

References

[1] Wang Y, Ruiz Diaz DF, Chen KS, Wang Z, Adroher XC. Materials, technological status, and fundamentals of PEM fuel cells – a review. Mater Today 2020;32:178–203.
[2] Ma R, Chai X, Geng R, Xu L, Xie R, Zhou Y, et al. Recent progress and challenges of multi-stack fuel cell systems: fault detection and reconfiguration, energy management strategies, and applications. Energy Convers Manag 2023;285.
[3] Tzelepis S, Kavadias KA, Marnellos GE, Xydis G. A review study on proton exchange membrane fuel cell electrochemical performance focusing on anode and cathode catalyst layer modelling at macroscopic level. Renew Sustain Energy Rev 2021;151.
[4] Pan Y, Wang H, Brandon NP. A fast two-phase non-isothermal reduced-order model for accelerating PEM fuel cell design development. Int J Hydrogen Energy 2022;47:38774–92.
[5] Weber AZ, Borup RL, Darling RM, Das PK, Dursch TJ, Gu W, et al. A Critical Review of Modeling Transport Phenomena in Polymer-Electrolyte Fuel Cells. J Electrochem Soc 2014;161:F1254–1F99.
[6] Zhao X, Zhou Y, Wang L, Pan B, Wang R, Wang L. Classification, summarization and perspective on modeling techniques for polymer electrolyte membrane fuel cell. Int J Hydrogen Energy 2023;48:21864–85.
[7] Bressel M, Hilairet M, Hissel D, Ould Bouamama B. Model-based aging tolerant control with power loss prediction of proton exchange membrane fuel cell. Int J Hydrogen Energy 2020;45:11242–54.
[8] Ziogou C, Voutetakis S, Georgiadis MC, Papadopoulou S. Model predictive control (MPC) strategies for PEM fuel cell systems – a comparative experimental demonstration. Chem Eng Res Design 2018;131:656–70.
[9] Wang N, Qu Z, Zhang G. Modeling analysis of polymer electrolyte membrane fuel cell with regard to oxygen and charge transport under operating conditions and hydrophobic porous electrode designs. eTransportation 2022;14.
[10] Yao J, Wu Z, Wang H, Yang F, Xuan J, Xing L, et al. Design and multi-objective optimization of low-temperature proton exchange membrane fuel cells with efficient water recovery and high electrochemical performance. Appl Energy 2022;324.
[11] Zhou Y, Meng K, Chen W, Deng Q, Chen B. Experimental performance of proton exchange membrane fuel cell with novel flow fields and numerical investigation of water-gas transport enhancement. Energy Convers Manag 2023;281.
[12] Vetter R, Schumacher JO. Free open reference implementation of a two-phase PEM fuel cell model. Comput Phys Commun 2019;234:223–34.
[13] Vetter R, Schumacher JO. Experimental parameter uncertainty in proton exchange membrane fuel cell modeling. Part I: scatter in material parameterization. J Power Sources 2019;438:227018.
[14] Vetter R, Schumacher JO. Experimental parameter uncertainty in proton exchange membrane fuel cell modeling. Part II: sensitivity analysis and importance ranking. J Power Sources 2019;439:126529.

[15] Zhang Y, He S, Jiang X, Fang H, Wang Z, Cao J, et al. Performance evaluation on full-scale proton exchange membrane fuel cell: mutual validation of one-dimensional, three-dimensional and experimental investigations. Energy Convers Manag 2024;299.
[16] Yao J, Yang Y, Hou X, Yang Y, Yang F, Wu Z, et al. Fast design of catalyst layer with optimal electrical-thermal-water performance for proton exchange membrane fuel cells. J Energy Chem 2023;81:642–55.
[17] Martín-Alcántara A, Pino J, Iranzo A. New insights into the temperature-water transport-performance relationship in PEM fuel cells. Int J Hydrogen Energy 2023;48:13987–99.
[18] García-Salaberri PA, Sánchez-Ramos A. Modeling of a polymer electrolyte membrane fuel cell with a hybrid continuum/discrete formulation at the rib/channel scale: effect of relative humidity and temperature on performance and two-phase transport. Appl Energy 2024;367.
[19] Xie B, Zhang G, Jiang Y, Wang R, Sheng X, Xi F, et al. 3D+1D" modeling approach toward large-scale PEM fuel cell simulation and partitioned optimization study on flow field. eTransportation 2020;6:100090.
[20] Falcão DS, Gomes PJ, Oliveira VB, Pinho C, Pinto AMFR. 1D and 3D numerical simulations in PEM fuel cells. Int J Hydrogen Energy 2011;36:12486–98.
[21] Cordiner S, Mulone V, Romanelli F. Thermal-fluid-dynamic simulation of a proton exchange membrane fuel cell using a hierarchical 3D-1D approach. J Fuel Cell Sci Technol 2007;4:317–27.
[22] Grimm M, Hellmann M, Kemmer H, Kabelac S. Interaction of cell flow directions and performance in PEM fuel cell systems following an anode based water management approach. J Power Sources 2023;580.
[23] Huo W, Wu P, Xie B, Du Q, Liang J, Qin Z, et al. Elucidating non-uniform assembling effect in large-scale PEM fuel cell by coupling mechanics and performance models. Energy Convers Manag 2023;277.
[24] Qin Z, Huo W, Bao Z, Tongsh C, Wang B, Du Q, et al. Alternating Flow Field Design Improves the Performance of Proton Exchange Membrane Fuel Cells. Adv Sci (Weinh) 2023;10:e2205305.
[25] Zheng L, Hou Y, Zhang T, Pan X. Performance prediction of fuel cells using long short-term memory recurrent neural network. Int J Energy Res 2021;45:9141–61.
[26] Wilberforce T, Olabi AG. Proton exchange membrane fuel cell performance prediction using artificial neural network. Int J Hydrogen Energy 2021;46:6037–50.
[27] Gu X, Hou Z, Cai J. Data-based flooding fault diagnosis of proton exchange membrane fuel cell systems using LSTM networks. Energy and AI 2021;4.
[28] Hua Z, Zheng Z, Péra M-C, Gao F. Remaining useful life prediction of PEMFC systems based on the multi-input echo state network. Appl Energy 2020;265.
[29] Ming W, Sun P, Zhang Z, Qiu W, Du J, Li X, et al. A systematic review of machine learning methods applied to fuel cells in performance evaluation, durability prediction, and application monitoring. Int J Hydrogen Energy 2023;48:5197–228.
[30] Feng S, Huang W, Huang Z, Jian Q. Optimization of maximum power density output for proton exchange membrane fuel cell based on a data-driven surrogate model. Appl Energy 2022;317.
[31] Legala A, Zhao J, Li X. Machine learning modeling for proton exchange membrane fuel cell performance. Energy AI 2022;10.
[32] Wang B, Yang Z, Ji M, Shan J, Ni M, Hou Z, et al. Long short-term memory deep learning model for predicting the dynamic performance of automotive PEMFC system. Energy AI 2023;14.
[33] Vaz N, Choi J, Cha Y, kong J, Park Y, Ju H. Multi-objective optimization of the cathode catalyst layer micro-composition of polymer electrolyte membrane fuel cells using a multi-scale, two-phase fuel cell model and data-driven surrogates. J Energy Chem 2023;81:28–41.
[34] Wang J, Jiang H, Chen G, Wang H, Lu L, Liu J, et al. Integration of multi-physics and machine learning-based surrogate modelling approaches for multi-objective optimization of deformed GDL of PEM fuel cells. Energy AI 2023;14.
[35] Wang B, Zhang G, Wang H, Xuan J, Jiao K. Multi-physics-resolved digital twin of proton exchange membrane fuel cells with a data-driven surrogate model. Energy AI 2020;1:100004.
[36] Zhang G, Wu L, Qin Z, Wu J, Xi F, Mou G, et al. A comprehensive three-dimensional model coupling channel multi-phase flow and electrochemical reactions in proton exchange membrane fuel cell. Adv Appl Energy 2021;2.
[37] Xie B, Ni M, Zhang G, Sheng X, Tang H, Xu Y, et al. Validation methodology for PEM fuel cell three-dimensional simulation. Int J Heat Mass Transf 2022;189.
[38] Chen Y-C, Karageorgiou C, Eller J, Schmidt TJ, Büchi FN. Determination of the porosity and its heterogeneity of fuel cell microporous layers by X-ray tomographic microscopy. J Power Sources 2022;539.
[39] Moein-Jahromi M, Kermani MJ. Performance prediction of PEM fuel cell cathode catalyst layer using agglomerate model. Int J Hydrogen Energy 2012;37:17954–66.
[40] Touhami S, Mainka J, Dillet J, Taleb SAH, Lottin O. Transmission line impedance models considering oxygen transport limitations in polymer electrolyte membrane fuel cells. J Electrochem Soc 2019;166:F1209–1F17.
[41] The United States Department of Energy. Appendix A- FCTT AST and polarization curve protocols for PEMFCs. (2013) https://www.energy.gov/eere/fuelcells/articles/fuel-cell-tech-team-accelerated-stress-test-and-polarization-curve.
[42] Tsotridis G, Pilenga A, Marco GD, Malkow T. EU harmonised test protocols for PEMFC MEA testing in single cell configuration for automotive applications. JRC Sci Policy Report 2015. https://doi.org/10.2790/54653. EUR 27632 EN.
[43] Peng Y, Choi J-Y, Bai K, Tian L, Pei K, Zhang Y, et al. Pitfalls of a commonly used accelerated stress test for reversal tolerance testing of proton exchange membrane fuel cell anode layers. J Power Sources 2024;596.